# New LTE-A Low-Latency Detectors for Cognitive Radio on Low-Cost FPGA SoC

Grégoire de Broglie, Louis Morge-Rollet, Denis Le Jeune, Frédéric Le Roy, Christian Roland, Charles Canaff, Jean-Philippe Diguet

▶ **To cite this version:**

Grégoire de Broglie, Louis Morge-Rollet, Denis Le Jeune, Frédéric Le Roy, Christian Roland, et al.. New LTE-A Low-Latency Detectors for Cognitive Radio on Low-Cost FPGA SoC. Journal of Signal Processing Systems, 2024, 10.1007/s11265-024-01932-9 . hal-04705309

**HAL Id: hal-04705309**
**https://hal.science/hal-04705309v1**

Submitted on 23 Sep 2024

**HAL** is a multi-disciplinary open access archive for the deposit and dissemination of scientific research documents, whether they are published or not. The documents may come from teaching and research institutions in France or abroad, or from public or private research centers.

L'archive ouverte pluridisciplinaire **HAL**, est destinée au dépôt et à la diffusion de documents scientifiques de niveau recherche, publiés ou non, émanant des établissements d'enseignement et de recherche français ou étrangers, des laboratoires publics ou privés.

# New LTE-A Low-Latency Detectors for Cognitive Radio on Low-Cost FPGA SoC

Grégoire de Broglie[1*], Louis Morge-Rollet[1], Denis Le Jeune[1], Frédéric Le Roy[1], Christian Roland[2], Charles Canaff[1], Jean-Philippe Diguet[3]

[1]Lab-STICC, ENSTA-Bretagne, 2, rue François Verny, Brest, 29806, Bretagne, France.
[2]Lab-STICC, Université Bretagne Sud, 27, rue Armand Guillemot, Lorient, 56321, Bretagne, France.
[3]IRL CROSSING, CNRS, 11 Victoria Dr, Adelaide, SA 5000, Australia.

*Corresponding author(s). E-mail(s): gregoire.de_broglie@ensta-bretagne.org;

**Abstract**

In this paper, we address the challenge of a real-time solution for the critical detection step in a cognitive radio (CR) network implemented using limited computing resources. The detection step is required to identify a free radio channel that can be used to transmit data. We first present two new detectors and their naive implementations on a CR platform running over LTE-advanced (LTE-A), an orthogonal frequency division multiple access (OFDMA) network. The first detection method is based on the subband's energy and the second uses both correlation on the cyclic prefix (CP)'s part and the energy of the useful orthogonal frequency division multiplexing (OFDM) signal. We then optimize them to satisfy with the low-latency detection constraints on a low-cost embedded board using a ZYNQ XC7Z020 system on a chip (SoC). We use Xilinx Vitis high-level synthesis (HLS) computer-aided design (CAD) tool to design our solutions. Finally we achieve the implementation of a solution that requires less than one OFDM symbol period (70 µs) for a detection system that complies with the worst scenario timing constraint of the LTE-A standard.

**Keywords:** LTE-A, Signal Detection, OFDM, HLS, Cognitive Radio

# 1 Introduction

## 1.1 Context

The aim of this work is to demonstrate that it is possible to build a stealth network on a public one by using CR technology with limited embedded computing resources. The goal of such a stealth network can be to utilize unused radio resources to control some drones without being detected. More precisely, we demonstrate here that real time detection of unused resources in a LTE-A cellular network is possible. Thus, it will be theoretically possible to develop a stealth network that tries to blend in with the mass of LTE-A transmissions.

The LTE-A standard uses the OFDMA multiplexing method, a technology inspired by the OFDM. The OFDM spreads the data on adjacent orthogonal frequency subcarriers making the information distributed on the time-frequency plane. OFDMA adds the possibility to assign a number of subcarriers to any of the users. An example of each of these technologies is shown in Figure 3a and Figure 3b. The LTE-A divides the plane in successive time-frequency units. The smallest unit is the resource block (RB), which contains 12 contiguous subcarriers and 7 successive temporal symbols. RBs are assigned by pairs by the evolved node B (eNodeB), the LTE-A relay antenna system, to the users of the network. The pairs of RBs are also called subframes. We can free ourself from this high-level of timing constraints with a low-cost platform like a Digilent Zedboard [1]. Despite the rise of the fifth generation (5G), the LTE-A will still be available for many years in the world, which makes it a long-term solution.

LTE-A downlink seems ideal for a CR system by its predictable structure if augmented with opportunistic capability. This supposes the design of a low-latency detector capable of finding the unused subframes and then, in an opportunistic way, occupy the unused subframes' time-frequencies resources with other communications, respecting the subframe's duration of 1 ms.

## 1.2 Challenge of Real-time Cognitive radio over LTE-A

Dynamic spectrum access is a major problem in telecommunications as it has been identified by the Federal Communications Commission (FCC) [2]. It involved many developments to solve it. One of them is a domain of the CR technology which seeks to use the free time-frequency spaces during the existing communications to send data of the other users. The licensed users are called primary users (PUs) and the other the secondary users (SUs). The first step of the CR (after the prior time and frequency synchronization to the network) is the detection of the PUs' communications.

This paper provides a solution to this problem for a particular case: the variant of the OFDMA adopted by LTE-A. Figure 1 shows an example of the LTE-A CR network. In our study, the SUs are low-power systems that could be embedded in Internet of things (IoT) devices and small drones. The signal's detection algorithms have to be as fast as possible and usable on a small platform with limited computing power. The devices will not communicate with the eNodeB to detect the free spaces in the LTE-A subband.

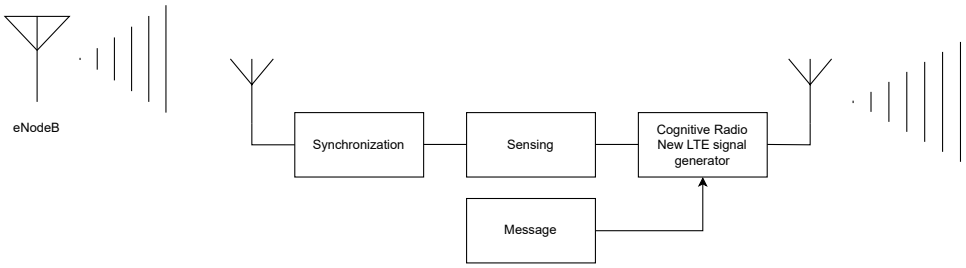


**Figure 1**: Schematic diagram of a LTE-A CR network

The LTE-A protocol divides the time-frequency plane in several subdivisions: the biggest time unit is the frame of 10 ms, divided in subframes, each of 1 ms, each itself divided in 2 RBs. Each RB is made of 7 OFDM temporal symbols and 12 subcarriers. The subcarriers are spaced by 15 kHz so, the bandwidth of the RB is equal to 180 kHz. The overall LTE-A bandwidth is divided in these RBs and a guard band on both sides of the bandwidth [3]. The subframe (i.e. a pair of RBs) is the data unit assigned to a user by the eNodeB for receiving data in a LTE-A network. The subframes of a frame can be independently used or not by the eNodeB to transmit data to network's users as illustrated in Figure 2. This constitutes a significant problem for the secondary network. Indeed, it needs to do the PUs' detection on each frequency subband and not on the whole LTE-A bandwidth. Moreover, the detection algorithms have to be very short because the full length of the LTE-A's unit is short: 1 ms. The CR platform analyzes the subframe for every subband, adds data that come from the buffer in the holes that have just been found and send the new waveform thus created with only secondary data.

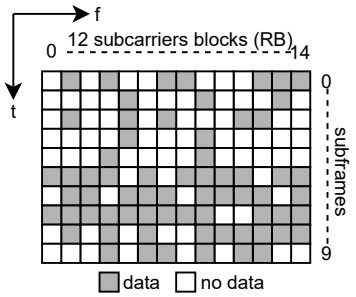


**Figure 2**: Example of a LTE-A group of subframes for a bandwidth of 3 MHz

A subframe starts by control data that can occupy at most the first 3 symbols over the 14 of a subframe. They are not correlated with the user data transmitted after. Furthermore, there is data in symbols $4^{\text{th}}$ to $14^{\text{th}}$ or not. So, if only noise is detected in the $4^{\text{th}}$ symbol, we know that we can transmit our data up to the end of the subframe. We can summarize our opportunistic CR process as follows: 1) we wait

for the $4^{\text{th}}$ symbol of a subframe to register it, 2) we do the detection's computations during the $5^{\text{th}}$ and 3) if there is none, we send our data from the $6^{\text{th}}$ to the $14^{\text{th}}$, the end of the subframes. So, if the computation is fast enough (i.e. roughly equal to 50 µs to let sufficient time to set up and send data from the buffer), we can have 9 temporal symbols and 12 subcarriers to transmit our data. The computation could be slower but at the expense of the communication time. We will finally recall that we use the Digilent ZedBoard [1] with the SoC ZYNQ XC7Z020-1CLG484C to show that the CR system can easily be embeddable on a platform with limited computing resources.

## 1.3 Contributions

We propose here the development and the implementation of two different detectors initially analyzed in [4]. These two new LTE-A signal detectors each require only one temporal symbol data to detect a transmission over a subframe period and one RB bandwidth (180 kHz) in a LTE-A time-frequency resources. The first works with the energy of the overall signal and the second one, called *eogration*, uses the correlation of the CP (the copied part of the signal, from its end to its beginning) and the energy of the remaining portion of the signal analyzed. This low data requirement for detection optimizes the free space usable by the secondary user.

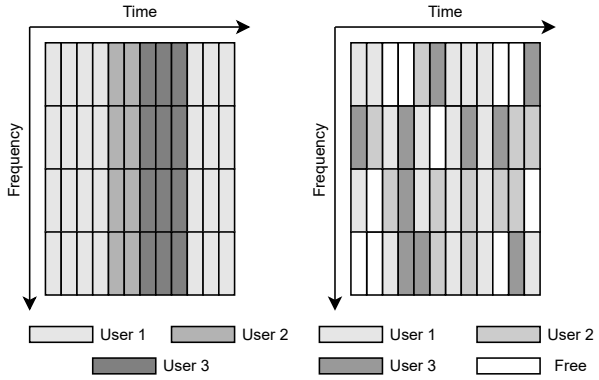


(a) OFDM (b) OFDMA

**Figure 3**: Resources allocation

The data detection algorithm used, following the normal frame detection and synchronization, follows a strict procedure. The first 3 symbols are control data and they are uncorrelated to the following user's transmitted payload, as detailed in [5]. We also know from the LTE-A standard, that the absence of data in the $4^{\text{th}}$ symbol implies no use of remaining symbols so an availability to our usage [5]. The faster the state of this symbol is known, the more data can be transmitted on the remaining free symbols. We developed the detectors to act only on one temporal symbol: the $4^{\text{th}}$ one.

We chose to implement the two detectors with Vitis HLS software from Xilinx [6] in a SoC XC7Z020-1CLG484C on the low-cost Digilent Zedboard [7]. It uses a C++

source code, pragmas, and preprocessing directives to translate the code into register transfer level (RTL) language. This design process allows the designer to go ahead with design space exploration whereas the classic process needs more handcraft coding to design the architecture of the intellectual property (IP). The fast Fourier transform (FFT) we used here comes from Xilinx IP libraries [8]. We tried different HLS optimizations to find a compromise between latency, hardware utilization resources, and the area occupied by the design.

The rest of the paper is organized as follows. First, we position this work in relation to the state of the art in Section 2. Section 3 describes the two detectors and their implementations. In Section 4, we present the optimizations to make them complying with our constraints. Section 5 details two studies. The first is the accuracy comparison between the computer's and the HLS' models to ensure that the decrease in precision is not significative. The second is about the architectures of the two detectors at each step of the optimization process to see how the optimizations impact the performances. Section 6 concludes the paper.

## 2 State of the art

The scarcity of the available electromagnetic spectrum, mentioned above, led to the idea of the CR technology by Mitola in [9]. The extensive use of OFDM modulation pushed the developments of many corresponding detectors, often implemented on field-programmable gate arrays (FPGAs).

Murty and Shrestha [10] also proposed the implementation of a wide-band frequency domain energy detector. This one computes an iterative FFT on 5-points to analyze a wideband signal with the help of the Goertzel's algorithm [11]. This work is unusable in our context because we need to analyse each RB bandwidth of the LTE-A subband and not only a few key points.

Ishwerya et al. in [12] and Kokkinen et al. in [13] used an autocorrelation instead of an energy detector. The first implementation especially worked on the compensation of the DC and frequency offsets, which is not a problem here because the LTE-A signal detector is already synchronized to the network of the eNodeB. The sensing time is too long, 414 µs, due to the data needed for the autocorrelation computation. Latter article has especially optimized the power consumption and the area usage. The computation time for small datasets, like 128 samples, is very fast, 9.6 µs, but the estimator cannot filter the RBs as it is. It should be added a filtering unit as we have done it in our estimators.

A random process $x(t)$ is known as wide-sense cyclostationary if its mean and autocorrelation are periodic. With a period $T_0$, they are denoted as follows

$$\mu(t) = \mu(t + T_0)$$
$$R_{xx}(t, \tau) = R_{xx}(t + T_0, \tau).$$

The autocorrelation is periodic, so it can be decomposed with a Fourier Series and denoted $R_x(t, \tau)$. We can derive from this the cyclic autocorrelation function (CAF)

$R_x^\alpha(\tau)$:

$$R_x(t,\tau) = \sum_{\alpha=-\infty}^{+\infty} R_x^\alpha e^{2i\pi\alpha t}$$

$$R_x^\alpha = \lim_{T\to+\infty} \frac{1}{T} \int_{-T/2}^{T/2} R_x(t,\tau) e^{-2i\pi\alpha t}\,\mathrm{d}t.$$

Allan et al. [14], Barakat et al. [15], and Murty et al. [16] described the optimized implementation of a cyclostationary detector for OFDM signals. The use of cyclostationary properties is inherently slow because of the time needed to determine the periodicity of the mean and the variance. So, despite the performance of the estimators, this type of detector does not fit with our requirements. These detectors needs, at least, two times more data than the one we designed to have the periodicity of the statistical properties.

Allan et al. [14], as [12], especially studied the effects of the impairments like carrier frequency offset (CFO), phase noise, in-phase and quadrature (I/Q) imbalance on the detection's performance. Barakat et al. [15] optimized the computation of cyclostationary sensing algorithms by using CORDIC scheme instead of complex computations as matrix inversion and FFT.

Finally, Chaurasiya et al. [17] showed a detector based on the eigenvalues of the OFDM signal, the theoretical aspects and the implementation on an FPGA. The sensing time is equal to 40 µs which is short, but only with a frequency of 400 MHz. It is understandable because the eigenvalue detector needs the signal's covariance matrix. Again, the detector is not designed to do the RB filtering simultaneously to the detection. So, we should add a independent filtering unit made by FFT and inverse fast Fourier transform (IFFT) blocks which disqualify this approach.

To the best of our knowledge, the existing solutions address the area optimization before the latency. We are considering the latency as the primary constraint to get access to all the available bandwidth. Then we improve our solution to minimize computing load and so resource used. Moreover, these solutions don't consider the RB filtering which is a key feature in our approach.

# 3 The detectors

## 3.1 The signal model

The downlink signal emitted by the eNodeB uses an OFDM modulator. This way, bits of communication data from the backbone network are merged to obtain complex symbol modulation like quadrature amplitude modulation (QAM). These symbols are then spread in an array like frequency data. An IFFT then changes them in time domain data. Finally, part of OFDM symbol's end is copied and placed to its beginning. This protects the signal from intersymbol interference (ISI) and makes it periodic, which is good for its equalization after the reception. This copy is called CP. The length of the symbol and the CP are respectively denoted $N$ and $N_{\mathrm{CP}}$. We know from [5] that $N_{\mathrm{CP}} \approx 0.07 \times N$ in LTE-A.

We will assume two things. First, as in [18, 19], the time domain data produced by the IFFT are independent and identically distributed (iid) random variables because they approximate a complex Gaussian process with independent real and imaginary parts. This is a good approximation confirmed by our results obtained with a generator which is working without this hypothesis. These results are showed in Section 3.5. Secondly, the propagation channel is non-dispersive and only adds white Gaussian noise to the original signal. There is no fast-fading or frequency selective fading. The first because all of the peripherals are motionless. The second because we assume the existence of a line of sight (LOS) between the eNodeB and the SU. So, with $n \in [\![0, N]\!]$ and $N \in \mathbb{N}^*$, the OFDM signal $s[n] \in \mathbb{C}$ is only affected by a constant attenuation coefficient denoted $h \in \mathbb{C}$ and a complex additive white Gaussian noise (AWGN) $w[n]$. We model the received signal by two hypotheses:

$$\begin{cases} \mathcal{H}_0 : x[n] = w[n] \\ \mathcal{H}_1 : x[n] = h \times s[n] + w[n]. \end{cases} \tag{1}$$

We ignore $h$ in the rest of the text due to its constant feature and note that $x[n] \in \mathbb{C}$. We have also the following density probabilities: $w[n] \sim \mathcal{CN}(0, \sigma_w^2)$ and $s[n] \sim \mathcal{CN}(0, \sigma_s^2)$.

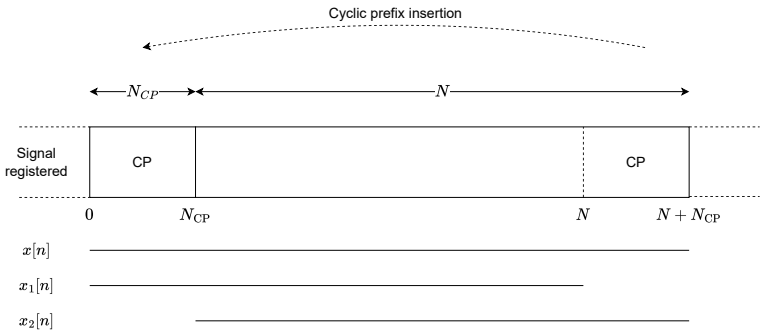


**Figure 4**: Two signals models.

Two signals $x_1[n]$ and $x_2[n]$ are extracted from the main one $x[n] \in \mathbb{C}$ as shown on Figure 4. They both have a length of $N$ samples and for $x[n]$, it is $N + N_{\mathrm{CP}}$. We consider that the whole signal $x[n]$ is stored before calculation. Lets $\mathrm{rect}_N(n)$ be the rectangular non-null function on $[\![-N/2, N/2]\!]$ interval. The equations of $x_1[n]$ and $x_2[n]$ are as follows:

$$\begin{cases} x_1[n] = x[n]\,\mathrm{rect}_N[n - N/2] \\ x_2[n] = x[n + N_{\mathrm{CP}}]\,\mathrm{rect}_N[n - N/2]. \end{cases} \tag{2}$$

## 3.2 Two detectors

Before the optimization and implementation steps, we come back on two of the three detectors we previously introduced in [4]: the energy and the *eogration* estimators. The first, as its name suggests, computes the energy of the received signal. The second correlates the repeated part and finds the energy of remaining signal. The detectors will be first analyzed for the detection of the whole LTE-A bandwidth and then, for one RB, i.e. a 180 kHz bandwidth. This will allow us to measure the effect of RB filtering on estimators' performances.

### 3.2.1 Energy estimator

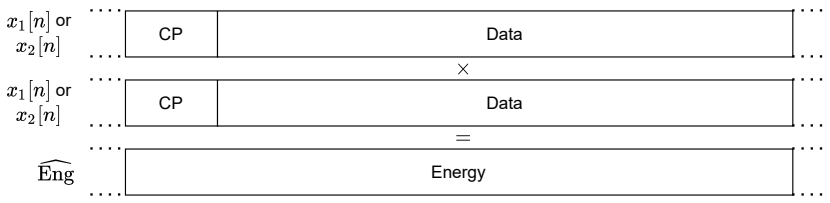


**Figure 5**: Working principle of energy estimator

Figure 5 is the working principle of the energy estimator. We first recall the canonical formula of an energy estimator for a complex signal $y[n], n \in [\![0, N]\!]$: $\sum_{n=0}^{N-1} |y[n]|^2 = \sum_{n=0}^{N-1} y[n] \cdot y^*[n]$. The detection is done in frequency domain by means of Parseval's identity. We use a complete useful OFDM signal $x_2[n]$ of $N$ samples. This one is used because it will be less affected by ISI than $x_1[n]$. The usage of FFT and IFFT preserves the OFDM's signal properties. The energy estimator is as follows:

$$\widehat{\text{Eng}}[m] = \underset{N \text{ points}}{\text{IDFT}} \left\{ \underset{N \text{ points}}{\text{DFT}} \{x_2\} \times \underset{N \text{ points}}{\text{DFT}} \{x_2\}^* \right\} \tag{3}$$

$$\widehat{\text{Eng}}[m] = \frac{1}{N} \sum_{n=0}^{N-1} \left( \sum_{k=0}^{N-1} x_2[k] e^{-2j\pi \frac{kn}{N}} \right) \left( \sum_{l=0}^{N-1} x_2[l] e^{-2j\pi \frac{ln}{N}} \right)^* e^{2j\pi \frac{nm}{N}} \tag{4}$$

$$\widehat{\text{Eng}}[m = 0] = \sum_{k=0}^{N-1} |x[k]|^2. \tag{5}$$

The proof of the previous equations is a part of the *eogration*'s demonstration available in Appendix A.1.

### 3.2.2 *Eogration* estimator

The *eogration* estimator does the frequency product of the circularly rotated conjugated signal $x_1$ and the signal $x_2$ as described in Figure 6. We also recall the correlation classical formula in time and frequency domains for 2 complex signals $x$ and $y$, a lag

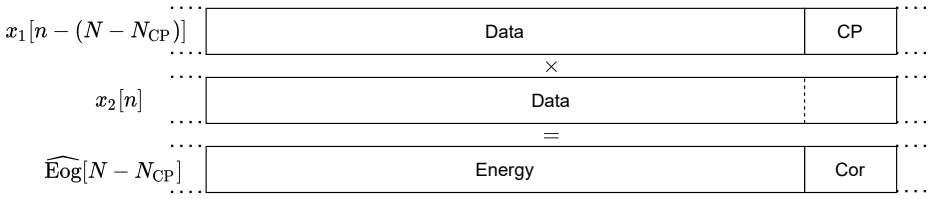


**Figure 6**: Working principle of *eogration* estimator

denoted $\tau$ and a frequency $f$: $R_{xy}[\tau] = \sum_{n=0}^{N-1} x[n+\tau]y^*[n]$ and $R_{xy}[f] = X[f]Y^*[f]$. As we show below, the *eogration*'s result is divided in two parts: the correlation and the energy.

$$\widehat{\text{Eog}}[m] = \underset{N \text{ points}}{\text{IDFT}} \left\{ \underset{N \text{ points}}{\text{DFT}} \{x_2\} \times \underset{N \text{ points}}{\text{DFT}} \{x_1\}^* \right\} \tag{6}$$

$$\widehat{\text{Eog}}[m] = \frac{1}{N} \sum_{n=0}^{N-1} \left( \sum_{k=0}^{N-1} x_2[k] e^{-2j\pi \frac{kn}{N}} \right) \left( \sum_{l=0}^{N-1} x_1[l] e^{-2j\pi \frac{ln}{N}} \right)^* e^{2j\pi \frac{nm}{N}} \tag{7}$$

$$\widehat{\text{Eog}}[m = N - N_{\text{CP}}] = \sum_{l=0}^{N_{\text{CP}}-1} x[l+N]x^*[l] + \sum_{l=N_{\text{CP}}}^{N-1} |x[l]|^2. \tag{8}$$

The demonstration of this result is located at Appendix A.1. The result of the *eogration* is a complex number and not the energy estimator. So, we take the real part of the *eogration*'s result:

$$\Re\left\{\widehat{\text{Eog}}[m = N - N_{\text{CP}}]\right\} = \Re\left\{ \sum_{l=0}^{N_{\text{CP}}-1} x[l+N]x^*[l] + \sum_{l=N_{\text{CP}}}^{N-1} |x[l]|^2 \right\} \tag{9}$$

$$\Re\left\{\widehat{\text{Eog}}[m = N - N_{\text{CP}}]\right\} = \sum_{l=0}^{N_{\text{CP}}-1} \Re\{x[l+N]x^*[l]\} + \sum_{l=N_{\text{CP}}}^{N-1} |x[l]|^2 \tag{10}$$

## 3.3 Comparison of the two estimators for the detection of whole bandwidth

### 3.3.1 Fisher's ratio

We use the Fisher's ratio to theoretically compare the performance of the estimators. The two hypotheses are seen as two classes and we want to keep them as separate as possible. This ratio has already been used in a similar contexts [20, 21]. The ratio takes into account the between-class and within-class variances. The ratio is defined as follows with $\mu_{\mathcal{H}_0}$ and $\sigma^2_{\mathcal{H}_0}$ the expected value and variance for null hypothesis ($\mathcal{H}_0$) and, $\mu_{\mathcal{H}_1}$ and $\sigma^2_{\mathcal{H}_1}$ the expected value and variance for alternative hypothesis ($\mathcal{H}_1$).

$$F = \frac{\left(\mu_{\mathcal{H}_0} - \mu_{\mathcal{H}_1}\right)^2}{\sigma^2_{\mathcal{H}_0} + \sigma^2_{\mathcal{H}_1}}. \tag{11}$$

**Table 1**: Statistics of the estimators

| | | $\Re\left\{\widehat{\text{Eng}}\right\}$ | $\Re\left\{\widehat{\text{Eog}}\right\}$ |
|---|---|---|---|
| $\mathcal{H}_0$ | $\mathbb{E}$ | $N\sigma_w^2$ | $(N - N_{\text{CP}})\sigma_w^2$ |
| | $\mathbb{V}$ | $N\left(\sigma_w^2\right)^2$ | $N_{\text{CP}}\left(\frac{\sigma_w^2}{\sqrt{2}}\right)^2 + (N - N_{\text{CP}})\left(\sigma_w^2\right)^2$ |
| $\mathcal{H}_1$ | $\mathbb{E}$ | $N(\sigma_s^2 + \sigma_w^2)$ | $N_{\text{CP}}\sigma_s^2 + (N - N_{\text{CP}})\left(\sigma_s^2 + \sigma_w^2\right)$ |
| | $\mathbb{V}$ | $N\left(\sigma_s^2 + \sigma_w^2\right)^2$ | $(N - N_{\text{CP}})(\sigma_s^2 + \sigma_w^2)^2 + N_{\text{CP}}\left(\left(\sigma_s^2\right)^2 + \sigma_s^2\sigma_w^2 + \left(\frac{\sigma_w^2}{\sqrt{2}}\right)^2\right)^2$ |
| Fisher ratio | | $N\frac{\left(\sigma_s^2\right)^2}{(\sigma_w^2)^2+(\sigma_s^2+\sigma_w^2)^2}$ | $\frac{\left(N\sigma_s^2\right)^2}{N(\sigma_s^2)^2+(2N-N_{\text{CP}})\sigma_s^2\sigma_w^2+(2N-N_{\text{CP}})(\sigma_w^2)^2}$ |

The results are showed in Table 1 and demonstrated in appendix A. We can see that the ratios of the energy and the *eogration* estimators are very close. It is consistent because the only difference between them is the correlation part of the *eogration*. However, it does not take into account some other statistical features like the asymmetry of the studied distribution or its kurtosis.

### 3.3.2 Simulations of the detection

To simulate the detectors, the signals $s[n]$ and $w[n]$ are randomly generated using the Gaussian hypotheses from section 3.1. Then, we create the CP for $s[n]$. The length of the signals for a 3 MHz in a LTE-A network is $N = 256$ and $N_{\text{CP}} = 18$ [3].

We simulate the two hypotheses $\mathcal{H}_0$ and $\mathcal{H}_1$ with 100 000 trials. This let us estimate their empirical distribution functions and deduce from the Dvoretzky-Kiefer-Wolfowitz (DKW) inequality [22, p. 99] a confidence band $\epsilon_n$ shown at Equation 12. The result is the following:

$$\epsilon_n = \sqrt{\frac{1}{2n}\ln\left(\frac{2}{\alpha}\right)} \tag{12}$$

$$\epsilon_n = 0.005, \tag{13}$$

for $n = 100\,000$ and $\alpha = 0.01$ (equivalent of a 99 % confidence band).

We set the false alarm rate of the hypothesis test to 5 %. For $\mathcal{H}_1$, we set, without loss of generality, the noise power $\sigma_w^2$ to 1 and modify the signal power $\sigma_s^2$ accordingly to the desired signal-to-noise ratio (SNR). We show the good detection probability plot (i.e. $\mathbb{P}(\hat{\mathcal{H}}_1|\mathcal{H}_1)$) in Figure 7 for a false alarm probability of 0.05. We also show the difference of performance detection between the two estimators on Figure 8. The energy performances are subtracted from the *eogration* performances. We see that the *eogration* estimator is at most 1.3 % better than the energy for a SNR of −9 dB.

We can see on Figure 9 that the CP length has a major effect on the *eogration*'s performance compared to the energy.

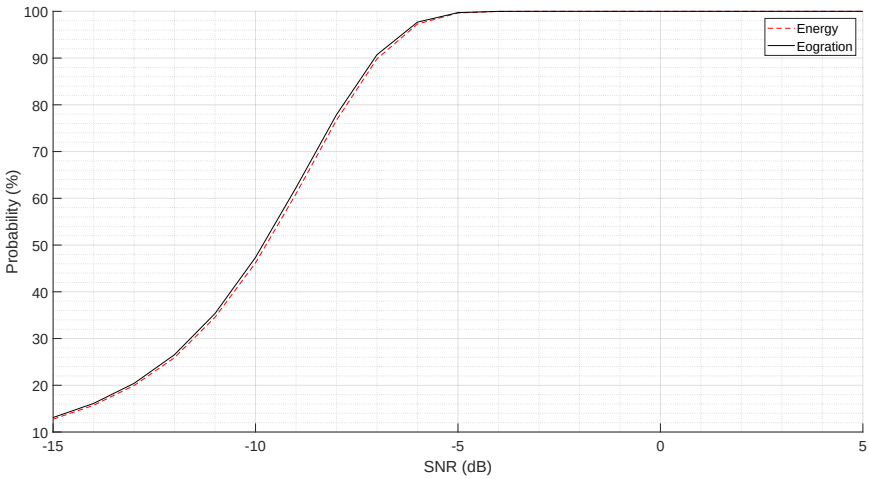


**Figure 7**: Probability of detection for a false alarm probability of 0.05

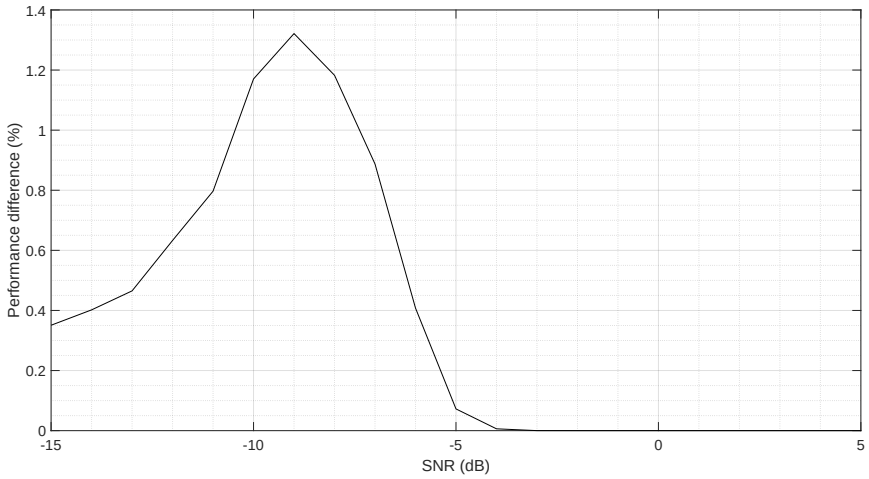


**Figure 8**: Difference of performance detection between energy and *eogration* estimator

## 3.4 Application to the detection of RB

### 3.4.1 The RB filtering

We study now the detectors' performance over a RB bandwidth. This is required because our proposed CR network seeks to exploit the unused RB in the LTE-A network. This also lets us study the declining performance when the frequency bandwidth is reduced. We recall first that a RB bandwidth is equivalent to 12 subcarriers. The frequency bins are all independent, so we can do a brick-wall filter by setting the useless ones to 0 in frequency domain. This is not a problem with the used Fourier transforms because of the rectangular windows they used. Indeed, the rectangular window

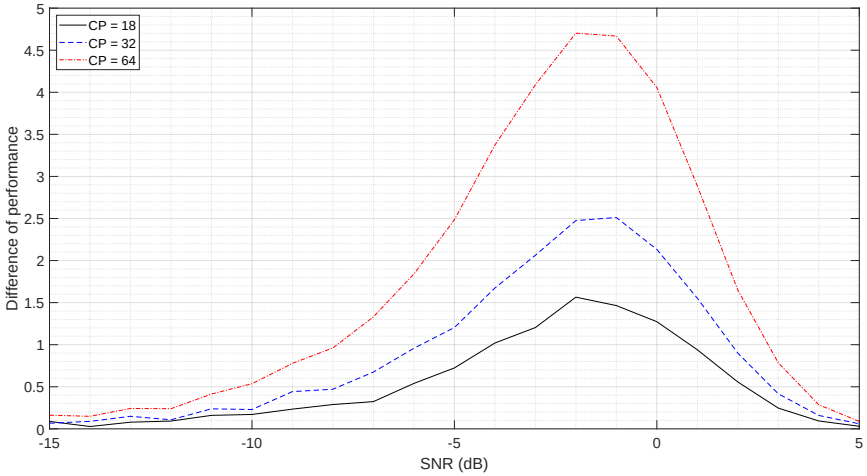


**Figure 9**: Difference of performance detection (in %) between energy and *eogration* for multiple CP lengths

creates sinc function and the OFDM's bins are all placed on its roots. The all bins are orthogonal in pairs. We present in Figure 10 and Figure 11 the two estimators with filtering blocks.

The S/P block maps data from serial to parallel. The FFTSHIFT block is a special one inspired by the function of the same name in MATLAB, due to the Cooley-Tukey FFT calculation algorithm. It reorders frequency array after the FFT to center the zero frequency of the spectrum. The FFT and IFFT are standards Fourier transform functions. The filtering block is a brick-wall filter.

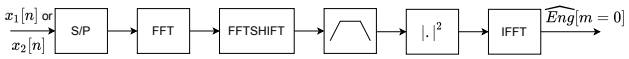


**Figure 10**: Block diagram of the energy estimator

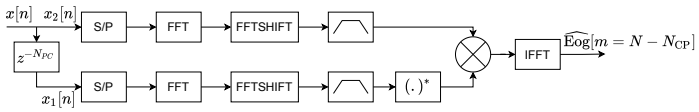


**Figure 11**: Block diagram of the *eogration* estimator

We can see the complexity gap between them. More precisely, the two branches for the two signals $x_1$ and $x_2$. So, we can deduce the increasing consumption of material resources and the relative latency's stability. This result is highlighted theoretically in Table 2 and empirically in Section 5 where we show the HLS synthesis' results.

**Table 2**: Compute complexity for a RB of 12 subcarriers

| Operator | multiplier | adder | conjugation |
|---|---|---|---|
| FFT & IFFT | $N/2\log_2 N$ | $N\log_2 N$ | 0 |
| $\|\ \|^2$ | 12 | 0 | 12 |
| $(\ )^*$ | 0 | 0 | 12 |
| multiplier operator | 12 | 0 | 0 |
| *Eogration* | $3N/2\log_2(N)+12$ | $3N\log_2(N)$ | 12 |
| *Eogration* ($N=1024$) | 15 372 | 30 720 | 12 |
| Energy | $N\log_2(N)+12$ | $2N\log_2(N)$ | 12 |
| Energy ($N=1024$) | 10 252 | 20 480 | 12 |

We define three computing units for our analysis: the complex adder and multiplier as well as the conjugation unit. The detectors are arbitrary set to a 10 MHz bandwidth to facilitate comparisons. It is equivalent to a value of $N = 1024$. So, we show that the *eogration* estimator requires approximately one third more multipliers and twice as much adders as the energy estimator.

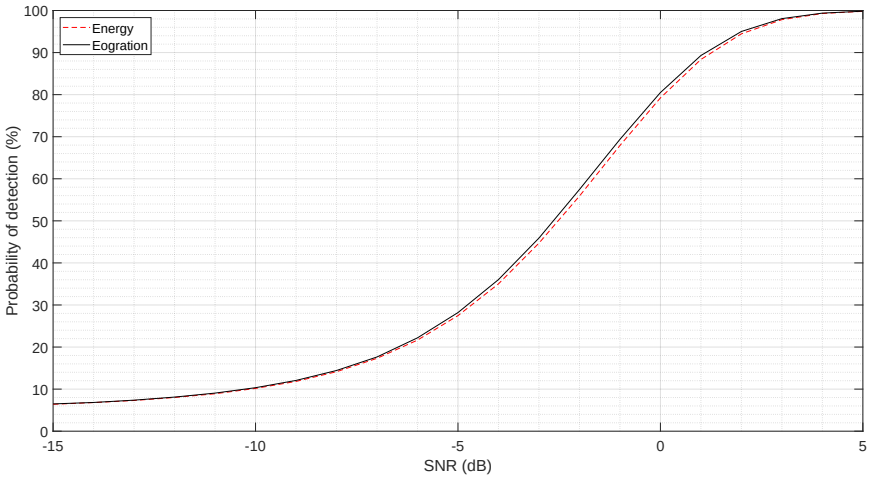


**Figure 12**: Estimators comparison for a CP of 18 samples, a symbol of 256 samples and on a RB subband

Figure 12 shows a performance drop of the estimators. This is perfectly understandable because they have much less data to process. For example, at $-5$ dB, the estimators on whole bandwidth achieve a detection probability of 1 and 0.29 for one RB bandwidth.

## 3.5 Simulations with a LTE-A signal generator

To confirm our signal model on Section 3.1, we also did the simulations with a more realistic software signal generator. Specifically, it complies with a part of the LTE-A

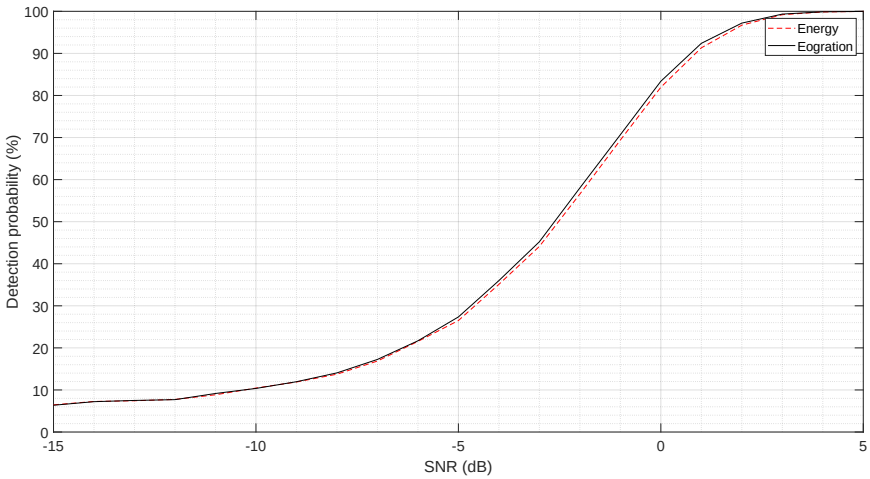


**Figure 13**: Estimators comparison for a CP of 18 samples on a 15 RBs subband with a more realistic model

standard as the frequency sampling, the FFT length, the guard band, the CP length, and the modulations used.

The possible frequencies are: 1.92 MHz, 3.84 MHz, 7.68 MHz, 15.36 MHz and 30.72 MHz. They respectively correspond to 6 RBs, 15 RBs, 25 RBs, 50 RBs, 75 RBs, and 100 RBs (the last two are both sampled at 30.72 MHz). The FFT length changes between 128 and 2048, and the guard band and the CP length depend on [3]. The modulation's list is quadrature phase shift-keying (QPSK), 16-QAM, and 64-QAM. Results are showed at Figure 13 for a 3.84 MHz bandwidth of 15 RBs with a CP of 18 samples.

These good performances show that our statistical hypothesis and our assumption on the samples independence are relevant.

# 4 Optimizations

As stated above, the energy and *eogration* estimators use one IFFT per analyzed RB at computation's end. Yet, a 10 MHz bandwidth has 50 RBs [23]. Therefore, 50 IFFTs are required for detection. So, these architectures are not usable as they stand. The FPGA on the Zedboard is not large enough and powerful to run these algorithms whether the RBs are sequentially or parallel analyzed. We show now how we succeeded in making them usable by means of mathematical optimizations. We also note that they will do not have any impact on the estimator's performance.

## 4.1 Optimization of the energy estimator

First, the filtering and square modulus units of Figure 10 are swapped. This allows to us to compute the square modulus only one time. Then, the set of filtering and IFFT computation is replaced by a new one which requires less resources. Firstly, the only

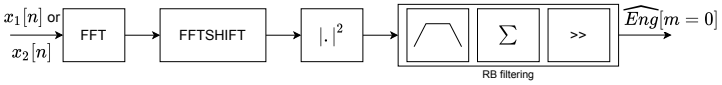


**Figure 14**: Block diagram of the optimized energy estimator.

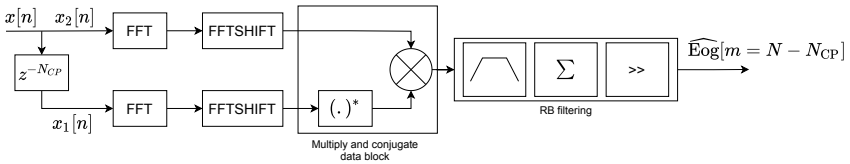


**Figure 15**: Block diagram of the optimized *eogration* estimator.

interesting instant is when $m = 0$ so, the IFFT becomes a sum of squared modulus. Secondly, because the unuseful subcarriers are set to 0 by the filter, the IFFT's sum can be reduced to the 12 subcarriers of the RB (the first subcarrier of the analyzed RB is denoted $n_{\text{RB}}$). Therefore the computation's complexity goes from $\mathcal{O}(N \log N)$ to $\mathcal{O}(1)$. Finally, the division by $N$ is replaced by a right bit shift due to the fact that $N$ is a power of 2. This is what is exposed below:

$$\widehat{\text{Eng}}[m] = \frac{1}{N} \sum_{k=0}^{N-1} |X[k]|^2 e^{2i\pi \frac{mk}{N}} \tag{14}$$

$$\widehat{\text{Eng}}[m=0] = \frac{1}{N} \sum_{k=0}^{N-1} |X[k]|^2 \tag{15}$$

$$\widehat{\text{Eng}}[m=0] = \frac{1}{N} \sum_{k=n_{\text{RB}}}^{n_{\text{RB}}+11} |X[k]|^2. \tag{16}$$

So, the filtering and the IFFT are substituted by a new single block easier to compute. The new block diagram is showed in Figure 14.

## 4.2 Optimization of the *eogration* estimator

As for the energy estimator, the IFFT part is a problem for the *eogration* estimator. It can be solved by seeing the IFFT as a matrix product with a matrix $\mathbf{W}$ of unity's roots as detailed in [24]. The IFFT is then written as: $\mathbf{x} = \mathbf{WX}$ where $\mathbf{x}$ is the temporal vector and $\mathbf{X}$ the frequency vector.

In the *eogration* estimator, we are only interested by one instant of the output: $m = N - N_{\text{CP}}$. This corresponds to only one line of $\mathbf{W}$. Furthermore, a RB filtering is done by selecting the 12 subcarriers it contains. From a matrix point of view, it is equivalent to extracting 12 columns in $\mathbf{W}$ and the corresponding 12 lines in $\mathbf{X}$. This

gives us the following result:

$$\widehat{\mathrm{Eog}}[m] = \frac{1}{N} \sum_{k=n_{\mathrm{RB}}}^{n_{\mathrm{RB}}+11} X[k] e^{2i\pi \frac{km}{N}} \tag{17}$$

$$\widehat{\mathrm{Eog}}\left[m = N - N_{\mathrm{CP}}\right] = \frac{1}{N} \sum_{k=n_{\mathrm{RB}}}^{n_{\mathrm{RB}}+11} X[k] e^{2i\pi \frac{k\times(N-N_{\mathrm{CP}})}{N}} \tag{18}$$

$$\widehat{\mathrm{Eog}}\left[m = N - N_{\mathrm{CP}}\right] = \frac{1}{N} e^{2i\pi n_{\mathrm{RB}} \frac{N-N_{\mathrm{CP}}}{N}} \times \sum_{k=0}^{11} X[k] e^{2i\pi \frac{k\times(N-N_{\mathrm{CP}})}{N}}. \tag{19}$$

We want to obtain the real part of this result. So, we need to precompute and store the exponentials of the analyzed RBs because we cannot take them out of the complex product. However, we note that $\frac{1}{N}$ still corresponds to a right bit shift. Figure 15 represents a simplified version of the detector in order to prepare the HLS implementation. The final result is the following:

$$\Re\left\{\widehat{\mathrm{Eog}}\left[m = N - N_{\mathrm{CP}}\right]\right\} = \frac{1}{N}\Re\left\{e^{2i\pi n_{\mathrm{RB}} \frac{N-N_{\mathrm{CP}}}{N}} \times \sum_{k=0}^{11} X[k] e^{2i\pi \frac{k\times(N-N_{\mathrm{CP}})}{N}}\right\}. \tag{20}$$

# 5 Design space exploration and analysis

We used the Xilinx Vitis HLS tool in version 2021.2 for the development of the two estimators. The FFT and IFFT IPs used here come from the fast Fourier transform (FFT) v9.1 LogiCORE IP from Xilinx. It is a RTL private code with a C++ interface to use it with the HLS. It is the reference IP of Xilinx for computing the FFT and it offers many possible configurations. Both estimators use a fixed-point architecture with 24 bits, as 23 bits are used as fractional part. The 24 bits configuration has been found by fine tuning and is sufficient to keep a good precision during the calculations.

## 5.1 Results comparison between Vitis HLS and computer's simulation

Design and simulation of the estimators have been done first with MATLAB and then, redone with Vitis HLS software. So, there is a need of a metric to compare the computer simulations working with *double* variables (denoted by $x_i$, $i \in [\![1, \ldots, n]\!]$) and the Vitis HLS simulations working with a fixed point 24 bits (denoted by $\hat{x}_i$, $i \in [\![1, \ldots, n]\!]$). First, we compute a root mean normalized square error (RMNSE). The normalization of the error is done by the reference value: the *double* results. Then, we deduce the number of significant bits from this result. The two formulas are the following:

$$\mathrm{RMNSE} = \sqrt{\frac{1}{N} \sum_{i=0}^{N-1} \frac{|x_i - \hat{x}_i|^2}{|x_i|^2}} \tag{21}$$

$$\text{Lost bits} = \lceil \log_2(\text{RMNSE}) + N_b \rceil, \tag{22}$$

where $N_b$ denotes the number of bits used during the computations, 24 here. So, the energy estimator loses 9 bits and the *eogration* 14 bits.

## 5.2 Performance and resources results

Synthesis results' are detailed in Table 3. They are divided in three parts. First, the original architectures with IFFT are used to analyze 1 RB. Second, the results of the optimized architectures are showed for the analyze of 1 RB. Finally, we show the results of the scaled optimized architectures, to analyze a typical 10 MHz bandwidth of 50 RBs as specified in LTE-A standard [23].

**Table 3**: Performance and resources utilizations (the units and the percents) of the estimators on a Digilent Zedboard at a clock frequency of 100 MHz for a 10 MHz LTE-A bandwidth

| Type of detectors | Math. optimized | With directives | Latency (cycles and time) | BRAM | DSP | FF | LUT |
|---|---|---|---|---|---|---|---|
| Energy | ✗ | ✗ | 10 585<br>105.85 µs | 36<br>(12 %) | 28<br>(12 %) | 14 503<br>(13 %) | 12 163<br>(22 %) |
| Energy | ✗ | ✓ | 9625<br>96.25 µs | 78<br>(27 %) | 58<br>(26 %) | 16 758<br>(15 %) | 17 056<br>(32 %) |
| Energy (1 RB) | ✓ | ✗ | 6355<br>63.55 µs | 24<br>(8 %) | 26<br>(11 %) | 13 909<br>(13 %) | 11 559<br>(22 %) |
| Energy (1 RB) | ✓ | ✓ | 5383<br>53.83 µs | 65<br>(23 %) | 56<br>(25 %) | 16 332<br>(15 %) | 15 156<br>(28 %) |
| Energy (50 RBs) | ✓ | ✗ | 6944<br>69.44 µs | 24<br>(8 %) | 26<br>(11 %) | 14 070<br>(13 %) | 11 756<br>(22 %) |
| Energy (50 RBs) | ✓ | ✓ | 5435<br>54.35 µs | 113<br>(40 %) | 56<br>(25 %) | 18 111<br>(17 %) | 16 969<br>(31 %) |
| *Eogration* | ✗ | ✗ | 11 596<br>115.96 µs | 61<br>(21 %) | 54<br>(24 %) | 28 163<br>(26 %) | 23 247<br>(43 %) |
| *Eogration* | ✗ | ✓ | 10 637<br>106.37 µs | 145<br>(51 %) | 114<br>(51 %) | 32 556<br>(30 %) | 31 145<br>(58 %) |
| *Eogration* (1 RB) | ✓ | ✗ | 6357<br>63.57 µs | 47<br>(16 %) | 58<br>(26 %) | 27 951<br>(26 %) | 22 947<br>(43 %) |
| *Eogration* (1 RB) | ✓ | ✓ | 5389<br>53.89 µs | 131<br>(46 %) | 142<br>(64 %) | 34 100<br>(32 %) | 32 776<br>(61 %) |
| *Eogration* (50 RBs) | ✓ | ✗ | 6946<br>69.46 µs | 47<br>(16 %) | 58<br>(26 %) | 28 261<br>(26 %) | 23 291<br>(43 %) |
| *Eogration* (50 RBs) | ✓ | ✓ | 5439<br>54.39 µs | 131<br>(46 %) | 162<br>(73 %) | 38 466<br>(36 %) | 36 095<br>(67 %) |

We can see that even for the analysis of 1 RB, the original architectures are inadequate because of too long computations with or without directives (more than 70 µs). This is due to the time needed by the sequential computations of the Fourier transforms. The optimized architectures for 1 RB are usable because they fulfill the

criteria defined before, that is the latencies are below 70 µs and they occupy a small part of the FPGA. This let the possibility to implement the rest of the CR system. We can see that the increase in latency of the scale up from 1 to 50 RBs is around 1 % because of the partial parallelism of the filtering unit, as shown in Table 5 and Table 6. The comparison of the estimators' architectures between 1 and 50 RBs is showed in Table 4.

**Table 4**: Comparison of the estimators for 1 and 50 RBs

| Detectors | Latency evolution (%) | BRAM evolution (%) | DSP evolution (%) | FF evolution (%) | LUT evolution (%) |
|---|---|---|---|---|---|
| Energy | 1 | 73 | 0 | 11 | 12 |
| *Eogration* | 1 | 0 | 14 | 13 | 10 |

We can also note that the *eogration* and the energy detectors have the same latency but do not need the same amount of resources. It is consistent because the two branches of the Figure 15 are executed in parallel. Then, the following blocks of the two detectors, which are the modulus and the conjugate blocks, are equivalent in terms of latency but not in resources. The modulus uses the real and the imaginary parts to do the computation, whereas the conjugate block needs digital signal processings (DSPs) units to work. Finally, the *eogration*'s RB filtering unit needs more resources than the energy estimator's one because of the unrolling of the multiply-add operation showed in Equation 19.

**Table 5**: Latency of energy's estimator optimized with and without directives

| Function | Without directives (in cycles) | With directives (in cycles) | Directives used | Algorithm n° |
|---|---|---|---|---|
| input buffer | 1026 | | ✗ | |
| FFT | 3195 | | ✗ | |
| FFTSHIFT | 1026 | | ✗ | |
| $\|.\|^2$ | 1028 | 68 | `#pragma HLS unroll factor=16`<br>`#pragma HLS array_partition type=cyclic factor=16` | 1 |
| RB filtering | 604 | 55 | `#pragma HLS unroll`<br>`#pragma HLS array_partition type=cyclic factor=16` | 2 |
| output buffer | 52 | | ✗ | |

The latency optimization's results of the two architectures are showed in Table 5 for energy and Table 6 for *eogration*, and the algorithms of the functions optimized by the directives are showed at Algorithms 1, 2, 3, and 4. The first parallelizes the

**Table 6**: Latency of *eogration*'s estimator optimized with and without directives

| Function | Without directives (in cycles) | With directives (in cycles) | Directives used | Algorithm n° |
|---|---|---|---|---|
| input buffer | 1026 | | ✗ | |
| FFT | 3195 | | ✗ | |
| FFTSHIFT | 1026 | | ✗ | |
| multiply & conjugate data block | 1026 | 68 | `#pragma HLS unroll factor=16`<br>`#pragma HLS array_partition type=cyclic factor=16` | 3 |
| RB filtering | 607 | 59 | `#pragma HLS unroll`<br>`#pragma HLS array_partition type=cyclic factor=16` | 4 |
| output buffer | 52 | | ✗ | |

**Algorithm 1** Modulus squared function

**Require:** Data ordered by FFTSHIFT function, $F = \{f_1, \ldots, f_N\}$ ▷ Partitioned array
**Require:** Modulus squared data, $M = \{m_1, \ldots, m_N\}$ ▷ Partitioned array
  **for** $i \leftarrow 0, N$ **do**
    $m_i = |f_i|^2$
  **end for**

squared modulus by unrolling the loop and dividing the arrays into smaller ones. As specified in Table 5, the loop is copied 16 times. The arrays division increases the amount of memory's ports and allows the competing access from the parallelized loops. The process is the same for the Algorithm 2: the 12 elements' sum is unrolled. This is why the latency of the filtering function is approximately equal to the amount of RBs. So, the latency of these two functions is respectively reduced by 93 % and 90 %.

As for the energy estimator, the Algorithms 3 and 4 divide the array and unroll the loop to reduce the computing's latency. The first unrolls 16 times the loop and does left bit shift in order to compensate the side effect of the multiplications on fixed point numbers. The Algorithm 4, as the Algorithm 2, unrolls the 12 elements' sum. The latency of this function is also roughly equal to the number of RBs. The latency of these two functions is reduced by 94 % and 90 %.

The three other non optimized functions of the two algorithms follow the same logic: the input buffer, the FFTSHIFT, and the output buffer are not unrolled and they process one sample per clock cycle. So, the optimized implementations comply with the constraints defined before: they can be embedded in a Digilent Zedboard with the SoC XC7Z020-1CLG484C and their respective latencies are below 70 µs.

**Algorithm 2** Filtering function for the energy estimator

**Require:** Modulus square data, $M = \{m_1, \ldots, m_N\}$ ▷ Partitioned array
**Require:** Filtered data, $F = \{f_1, \ldots, f_{N_{\mathrm{RB}}}\}$ ▷ Partitioned array
  **for** $i \leftarrow 0, N_{\mathrm{RB}}$ **do** ▷ Not unrolled loop
    **for** $j \leftarrow 0, 12$ **do** ▷ Unrolled loop
      **if** $j = 0$ **then**
        $sum = 0$
        $index = 212 + i \times 12$
      **end if**
      $sum = sum + m_{index+j}$
      **if** $j = 11$ **then**
        $f_i = sum \times 2$
      **end if**
    **end for**
  **end for**

**Algorithm 3** Multiply and conjugate function

**Require:** First signal $X = \{x_1, \ldots, x_N\}$ ▷ Partitioned array
**Require:** Second signal $Y = \{y_1, \ldots, y_N\}$ ▷ Partitioned array
**Require:** Data multiplied and conjugated, $O = \{o_1, \ldots, o_N\}$ ▷ Partitioned array
  **for** $i \leftarrow 0, N$ **do** ▷ Unrolled loop
    $o_i = x_i^* \times y_i$
    $o_i = o_i << 9$
  **end for**

# 6 Conclusion

We presented here the design, optimization, and implementation of two new detectors designed to work in a LTE-A opportunistic CR network. They are the first brick of a CR system based on the reuse of the free spaces in the LTE-A network. The first algorithm computes the energy of the whole signal. The second does also the energy's computation, but of the useful symbol and the correlation of the CP part. The targeted platform in this paper is the Digilent ZedBoard with the SoC XC7Z020-1CLG484C. The latency's goal is below 70 µs to make the detection shorter than one OFDM symbol transmission, which maximizes the amount of data transmitted in the white spaces of the LTE-A. The CAD tool used for this work is Vitis-HLS 2021.2 from Xilinx and the FFT v9.1 LogiCORE IP from Xilinx. We first mathematically optimized our algorithms. Secondly, we used high-level preprocessing directives like *array partition* and *unroll* to perform design space exploration and select enhanced architectures on FPGA. We achieved to find and implement solutions that meet the real time constraints on a low cost FPGA board. So we demonstrated the possibility to create an opportunistic stealth network based on a real time detection of empty slot that allows a full use of the available free bandwidth while using low cost FPGA board. This is possible because the critical step in terms of latency is the detection.

**Algorithm 4** Filtering function for the *eogration* estimator

**Require:** Multiplied data, $M = \{m_1, \ldots, m_N\}$ ▷ Partitioned array
**Require:** Exponential table of the 12 subcarriers, $E = \{e_1, \ldots, e_{12}\}$
**Require:** Filtered data, $F = \{f_1, \ldots, f_{N_{\mathrm{RB}}}\}$ ▷ Partitioned array
  **for** $i \leftarrow 0$, $N_{\mathrm{RB}}$ **do** ▷ Not unrolled loop
    **for** $j \leftarrow 0$, 12 **do** ▷ Unrolled loop
      **if** $j = 0$ **then**
        $sum = 0$
        $index = 212 + i \times 12$
      **end if**
      $sum = sum + m_{index+j} \times e_j$
      **if** $j = 12$ **then**
        $f_i = |sum|^2$
      **end if**
    **end for**
  **end for**

The other steps as the design of an IP that spreads the secondary user's data into the white spaces previously found in the LTE-A network can be implemented with available resources. Thus, the whole platform will constitute a proof that the design of an opportunistic embeddable emitter is possible even with a low-cost system. We can also search how to transpose the results obtained to other OFDMA networks or maybe to 5G network to make this CR network more widespread. The 5G network is a potential lead because some standard configurations are very similar to the LTE-A in order to make the transition easier.

# Appendix A Detailed computations of the *eogration*

## A.1 Developed form of the *eogration* estimator

We compute here the *eogration* estimator described in 3.2.2.

$$\widehat{\mathrm{Eog}}[m] = \frac{1}{N}\sum_{n=0}^{N-1}\left(\sum_{k=0}^{N-1} x_2[k]e^{-2j\pi\frac{kn}{N}}\right) \left(\sum_{l=0}^{N-1} x_1[l]e^{-2j\pi\frac{ln}{N}}\right)^* e^{2j\pi\frac{nm}{N}} \tag{A1}$$

$$\widehat{\mathrm{Eog}}[m] = \sum_{k=0}^{N-1}\sum_{l=0}^{N-1} x_2[k]x_1^*[l]\left(\frac{1}{N}\sum_{n=0}^{N-1} e^{-2j\pi\frac{((k-l)-m)n}{N}}\right). \tag{A2}$$

At the moment $m = N - N_{\mathrm{CP}}$ the mean sum of exponentials is equal to 1 when $k - l = N - N_{\mathrm{CP}}$ or $k = l + (N - N_{\mathrm{CP}})$, so we have:

$$\widehat{\mathrm{Eog}}[m = N - N_{\mathrm{CP}}] = \sum_{k=0}^{N-1} \sum_{l=0}^{N-1} x_2[k] x_1^*[l] \delta[(k-l) - (N - N_{\mathrm{CP}})] \tag{A3}$$

$$= \sum_{k=0}^{N-1} x_2[l + (N - N_{\mathrm{CP}})] x_1^*[l] \tag{A4}$$

$$= \sum_{l=0}^{N_{\mathrm{CP}}-1} x_2[l + (N - N_{\mathrm{CP}})] x_1^*[l] \tag{A5}$$

$$= \sum_{l=0}^{N_{\mathrm{CP}}-1} x[l + N] x^*[l]. \tag{A6}$$

For $k = l - N_{\mathrm{CP}}$, we have:

$$\widehat{\mathrm{Eog}}[m = N - N_{\mathrm{CP}}] = \sum_{k=0}^{N-1} \sum_{l=0}^{N-1} x_2[k] x_1^*[l] \delta[(k-l) - (N - N_{\mathrm{CP}}) + N] \tag{A7}$$

$$= \sum_{l=0}^{N-1} x_2[l - N_{\mathrm{CP}}] x_1^*[l] \tag{A8}$$

$$= \sum_{l=N_{\mathrm{CP}}}^{N-1} x_2[l - N_{\mathrm{CP}}] x_1^*[l] \tag{A9}$$

$$= \sum_{l=N_{\mathrm{CP}}}^{N-1} |x[l]|^2. \tag{A10}$$

So, we obtain the following estimator:

$$\widehat{\mathrm{Eog}}[m = N - N_{\mathrm{CP}}] = \sum_{l=0}^{N_{\mathrm{CP}}-1} x[l + N] x^*[l] + \sum_{l=N_{\mathrm{CP}}}^{N-1} |x[l]|^2. \tag{A11}$$

The correlated part of the Equation A11 is a complex number whereas the energy is a real number. So, we take the real part of the correlation. Hence, we rewrite the equation as follows:

$$\Re\left\{\widehat{\mathrm{Eog}}[m = N - N_{\mathrm{CP}}]\right\} = \Re\left\{\sum_{l=0}^{N_{\mathrm{CP}}-1} x[l + N] x^*[l]\right\} + \sum_{l=N_{\mathrm{CP}}}^{N-1} |x[l]|^2 \tag{A12}$$

$$\Re\left\{\widehat{\mathrm{Eog}}[m = N - N_{\mathrm{CP}}]\right\} = \sum_{l=0}^{N_{\mathrm{CP}}-1} \Re\left\{x[l+N]x^*[l]\right\} + \sum_{l=N_{\mathrm{CP}}}^{N-1} |x[l]|^2. \tag{A13}$$

## A.2 Computation of the statistical features

We are seeking the statistical features of the *eogration* estimator. These results will be partially reused by the energy estimator because of the second part of the Equation A11.

### A.2.1 The variance of a complex sum of random variables

The formula of a variance of a sum of complex random variables is the following:

$$\mathbb{V}\left\{\sum_{k=1}^{N} a_k Z_k\right\} = \sum_{k=1}^{N}\sum_{l=1}^{N} a_k \overline{a_l}\,\mathrm{Cov}\{Z_k, Z_l\}, \tag{A14}$$

with a complex random variable denoted $Z_k$ and the coefficients $a_k$.

The covariances produced by the computation of the *eogration* estimator's variance are null. So, the variance of the sum is equal to the sum of the variance. In other words:

$$\mathbb{V}\left\{\Re\left\{\widehat{\mathrm{Eog}}\right\}\right\} = \sum_{l=0}^{N_{\mathrm{CP}}-1} \mathbb{V}\left\{\Re\{x[l+N]x^*[l]\}\right\} + \sum_{l=N_{\mathrm{CP}}}^{N-1} \mathbb{V}\left\{|x[l]|^2\right\}. \tag{A15}$$

### A.2.2 Null hypothesis

***The expected value***

We are computing the expected value of the estimator for the null hypothesis (i.e. when there is only noise):

$$\mathbb{E}\left\{\Re\left\{\widehat{\mathrm{Eog}}[m = N - N_{\mathrm{CP}}]\right\}\right\} = \mathbb{E}\left\{\sum_{l=0}^{N_{\mathrm{CP}}-1} \Re\{x[l+N]x^*[l]\} + \sum_{l=N_{\mathrm{CP}}}^{N-1} |x[l]|^2\right\} \tag{A16}$$

$$\mathbb{E}\left\{\Re\left\{\widehat{\mathrm{Eog}}[m = N - N_{\mathrm{CP}}]\right\}\right\} = \sum_{l=N_{\mathrm{CP}}}^{N-1} \sigma_w^2 \tag{A17}$$

$$\mathbb{E}\left\{\Re\left\{\widehat{\mathrm{Eog}}[m = N - N_{\mathrm{CP}}]\right\}\right\} = (N - N_{\mathrm{CP}})\sigma_w^2. \tag{A18}$$

***The variance***

We compute the variance of the *eogration*:

$$\mathbb{V}\left\{\Re\left\{\widehat{\mathrm{Eog}}\right\}\right\} = \sum_{l=0}^{N_{\mathrm{CP}}-1} \mathbb{V}\left\{\Re\{x[l+N]x^*[l]\}\right\} + \sum_{l=N_{\mathrm{CP}}}^{N-1} \mathbb{V}\left\{|x[l]|^2\right\} \tag{A19}$$

$$\mathbb{V}\left\{\Re\left\{\widehat{\mathrm{Eog}}\right\}\right\} = N_{\mathrm{CP}}\left(\frac{\sigma_w^2}{\sqrt{2}}\right)^2 + (N - N_{\mathrm{CP}})\left(\sigma_w^2\right)^2. \tag{A20}$$

### A.2.3 Alternative hypothesis

***Expected value***

We compute here the expected values of the two parts of the *eogration* estimator's real part:

$$\mathbb{E}\left\{\Re\left\{\widehat{\mathrm{Eog}}[m = N - N_{\mathrm{CP}}]\right\}\right\} = \mathbb{E}\left\{\sum_{l=0}^{N_{\mathrm{CP}}-1} \Re\{x[l+N]x^*[l]\} + \sum_{l=N_{\mathrm{CP}}}^{N-1} |x[l]|^2\right\} \tag{A21}$$

$$\mathbb{E}\left\{\Re\left\{\widehat{\mathrm{Eog}}[m = N - N_{\mathrm{CP}}]\right\}\right\} = \sum_{l=0}^{N_{\mathrm{CP}}-1} \sigma_s^2 + \sum_{l=N_{\mathrm{CP}}}^{N-1} \left(\sigma_s^2 + \sigma_w^2\right) \tag{A22}$$

$$\mathbb{E}\left\{\Re\left\{\widehat{\mathrm{Eog}}[m = N - N_{\mathrm{CP}}]\right\}\right\} = N_{\mathrm{CP}}\sigma_s^2 + (N - N_{\mathrm{CP}})\left(\sigma_s^2 + \sigma_w^2\right) \tag{A23}$$

***Variance***

We compute the variance of the *eogration* estimator's real part for the alternative hypothesis:

$$\mathbb{V}\left\{\Re\left\{\widehat{\mathrm{Eog}}\right\}\right\} = \sum_{l=0}^{N_{\mathrm{CP}}-1} \mathbb{V}\left\{\Re\{x[l+N]x^*[l]\}\right\} + \sum_{l=N_{\mathrm{CP}}}^{N-1} \mathbb{V}\left\{|x[l]|^2\right\} \tag{A24}$$

$$\mathbb{V}\left\{\Re\left\{\widehat{\mathrm{Eog}}\right\}\right\} = (N - N_{\mathrm{CP}})\left(\sigma_s^2 + \sigma_w^2\right)^2 + N_{\mathrm{CP}}\left(\left(\sigma_s^2\right)^2 + \sigma_s^2\sigma_w^2 + \left(\frac{\sigma_w^2}{\sqrt{2}}\right)^2\right) \tag{A25}$$

## A.3 Statistical features of the two estimators

### A.3.1 The energy estimator

The statistical features of the energy estimator are deduced from the previous results:

$$\mathcal{H}_0 \begin{cases} \mathbb{E}\left\{\sum_{n=0}^{N-1} |x[n]|^2\right\} &= N\sigma_w^2 \\ \mathbb{V}\left\{\sum_{n=0}^{N-1} |x[n]|^2\right\} &= N\left(\sigma_w^2\right)^2 \end{cases} \tag{A26}$$

$$\mathcal{H}_1 \begin{cases} \mathbb{E}\left\{\sum_{n=0}^{N-1} |x[n]|^2\right\} &= N\left(\sigma_s^2 + \sigma_w^2\right) \\ \mathbb{V}\left\{\sum_{n=0}^{N-1} |x[n]|^2\right\} &= N\left(\sigma_s^2 + \sigma_w^2\right)^2 \end{cases} \tag{A27}$$

### A.3.2 The *eogration* estimator

This equation summarize the results obtained previously:

$$\mathcal{H}_0 \begin{cases} \mathbb{E}\left\{\Re\left\{\widehat{\mathrm{Eog}}[m = N - N_{\mathrm{CP}}]\right\}\right\} = (N - N_{\mathrm{CP}})\sigma_w^2 \\ \mathbb{V}\left\{\Re\left\{\widehat{\mathrm{Eog}}[m = N - N_{\mathrm{CP}}]\right\}\right\} = N_{\mathrm{CP}}\left(\frac{\sigma_w^2}{\sqrt{2}}\right)^2 + (N - N_{\mathrm{CP}})\left(\sigma_w^2\right)^2 \end{cases} \tag{A28}$$

$$\mathcal{H}_1 \begin{cases} \mathbb{E}\left\{\Re\left\{\widehat{\mathrm{Eog}}[m = N - N_{\mathrm{CP}}]\right\}\right\} = N_{\mathrm{CP}}\sigma_s^2 + (N - N_{\mathrm{CP}})(\sigma_s^2 + \sigma_w^2) \\ \mathbb{V}\left\{\Re\left\{\widehat{\mathrm{Eog}}[m = N - N_{\mathrm{CP}}]\right\}\right\} = (N - N_{\mathrm{CP}})\left(\sigma_s^2 + \sigma_w^2\right)^2 + N_{\mathrm{CP}}\left(\left(\sigma_s^2\right)^2 + \sigma_s^2\sigma_w^2 + \left(\frac{\sigma_w^2}{\sqrt{2}}\right)^2\right) \end{cases} \tag{A29}$$

# References


[1] Avnet: ZedBoard | Avnet Boards. https://www.avnet.com/wps/portal/us/products/avnet-boards/avnet-board-families/zedboard/zedboard-board-family/

[2] Federal Communications Commission: Spectrum Policy Task Force. https://www.fcc.gov/document/spectrum-policy-task-force (2015)

[3] 3GPP: Specification # 36.104. https://portal.3gpp.org/desktopmodules/Specifications/SpecificationDetails.aspx?specificationId=2412

[4] de Broglie, G., Morge-Rollet, L., Le Jeune, D., Le Roy, F., Roland, C., Canaff, C., Diguet, J.-P.: New Methods for Fast Detection for Embedded Cognitive Radio. In: 2022 Asia-Pacific Signal and Information Processing Association Annual Summit and Conference (APSIPA ASC), pp. 2007–2014 (2022). https://doi.org/10.23919/APSIPAASC55919.2022.9980109

[5] Ghosh, A., Zhang, J., Andrews, J.G., Muhamed, R.: Fundamentals of LTE. Prentice Hall, Upper Saddle River, NJ (2010)

[6] Xilinx: Getting Started with Vitis HLS • Vitis High-Level Synthesis User Guide (UG1399) • Reader • Documentation Portal. https://docs.xilinx.com/r/en-US/ug1399-vitis-hls

[7] Digilent: ZedBoard - Digilent Reference. https://digilent.com/reference/programmable-logic/zedboard/start?redirect=1

[8] Xilinx: Fast Fourier Transform v9.1 LogiCORE IP Product Guide, 98 (2021)

[9] Mitola, J., Maguire, G.Q.: Cognitive radio: Making software radios more personal. IEEE Pers. Commun. **6**(4), 13–18 (Aug./1999) https://doi.org/10.1109/98.788210

[10] Murty, M.S., Shrestha, R.: Hardware-Efficient and Wide-Band Frequency-Domain Energy Detector for Cognitive-Radio Wireless Network. In: 2018 31st International Conference on VLSI Design and 2018 17th International Conference on Embedded Systems (VLSID), pp. 277–282 (2018). https://doi.org/10.1109/VLSID.2018.76

[11] Mitra, S.K.: Digital Signal Processing: A Computer-Based Approach, 3. ed., international ed edn. Mcgraw-Hill Series in Electrical and Computer Engineering. McGRAW-HILL, Boston (2006)

[12] Ishwerya, P., Geethu, S., Lakshminarayanan, G.: Autocorrelation based spectrum sensing architecture on FPGA with dynamic offset compensation. In: 2016 IEEE International Conference on Distributed Computing, VLSI, Electrical Circuits and Robotics, DISCOVER 2016 - Proceedings, pp. 153–157 (2016). https://doi.org/10.1109/DISCOVER.2016.7806250

[13] Kokkinen, K., Turunen, V., Kosunen, M., Chaudhari, S., Koivunen, V., Ryynänen, J.: On the implementation of autocorrelation-based feature detector. In: 2010 4th International Symposium on Communications, Control and Signal Processing (ISCCSP), pp. 1–4 (2010). https://doi.org/10.1109/ISCCSP.2010.5463304

[14] Allan, D., Crockett, L., Weiss, S., Stuart, K., Stewart, R.W.: FPGA implementation of a cyclostationary detector for OFDM signals. In: 2016 24th European Signal Processing Conference (EUSIPCO), pp. 647–651 (2016). https://doi.org/10.1109/EUSIPCO.2016.7760328

[15] Barakat, M., Saad, W., Shokair, M.: FPGA Implementation of Cyclostationary Feature Detector for Cognitive Radio OFDM Signals. In: 2018 13th International Conference on Computer Engineering and Systems (ICCES), pp. 215–218. IEEE, Cairo (2018). https://doi.org/10.1109/ICCES.2018.8639225

[16] Murty, M.S., Shrestha, R.: VLSI Architecture for Cyclostationary Feature Detection Based Spectrum Sensing for Cognitive-Radio Wireless Networks and Its ASIC Implementation. In: 2016 IEEE Computer Society Annual Symposium on VLSI (ISVLSI), pp. 69–74 (2016). https://doi.org/10.1109/ISVLSI.2016.12

[17] Chaurasiya, R.B., Shrestha, R.: Fast Sensing-Time and Hardware-Efficient Eigenvalue-Based Blind Spectrum Sensors for Cognitive Radio Network. IEEE Transactions on Circuits and Systems I: Regular Papers **67**(4), 1296–1308 (2020) https://doi.org/10.1109/TCSI.2019.2941762

[18] van de Beek, J.J., Sandell, M., Borjesson, P.O.: ML estimation of time and frequency offset in OFDM systems. IEEE Trans. Signal Process. **45**(7), 1800–1805 (1997) https://doi.org/10.1109/78.599949

[19] Sesia, S., Toufik, I., Baker, M.: LTE, The UMTS Long Term Evolution: From Theory to Practice, 1st edn. (2009)

[20] Li, C., Wang, B.: Fisher Linear Discriminant Analysis. CCIS Northeastern University (2014)

[21] Zarka, J., Guth, F., Mallat, S.: Separation and Concentration in Deep Networks. arXiv:2012.10424 [cs] (2021)

[22] Wasserman, L.: All of Statistics A Concise Course in Statistical Inference. Springer Texts in Statistics. Springer, New York (2004)

[23] 3GPP: Norme 3GPP 36.104 - V9.1.0 - Release 9 - Base Station Radio Transmission and Reception. 3GPP

[24] Rao, K.R., Yip, P.: The Transform and Data Compression Handbook, 1st edn. The Electrical Engineering and Signal Processing Series. CRC Press, Boca Raton, Fla (2001)